Post-print
Submitted, accepted and published in: International Journal Of Hydrogen Energy, 3698-3709 (2014); DOI:10.1016/j.ijhydene.2013.12.127

Hydrogen and Multiwall Carbon Nanotubes production by Catalytic Decomposition of Methane: thermogravimetric analysis and scaling-up of Fe-Mo catalysts

D. Torres, J.L. Pinilla, M.J. Lázaro, R. Moliner, I. Suelves*

Instituto de Carboquímica, CSIC, Miguel Luesma Castán 4, 50018 Zaragoza, Spain

Abstract

Fe-based catalysts doped with Mo were prepared and tested in the catalytic decomposition of methane (CDM), which aims for the co-production of CO_2-free hydrogen and tubular nanostructured carbon (NC). Catalysts performance were tested in a thermobalance operating either at isothermal or temperature programmed mode by monitoring the weight changes with time or temperature, respectively, as a result of NC growth on the metal particles. Maximum performance of Fe-Mo catalysts was found at the temperature range of 700-900ºC. The addition of Mo as dopant resulted in an increase in the rate and amount of deposited carbon, reaching an optimum in the range 2.5-7.5% (mol) of MoO_3 for Fe-Mo/Al_2O_3 catalysts, whereas for Fe-Mo/MgO catalyst an optimum at 7.5 % MoO_3 loading was obtained. XRD study revealed the effect of the Mo addition on the Fe_2O_3/Fe crystal domain size in the fresh and reduced catalysts. Tubular carbon nanostructures with high structural order were obtained using Fe-Mo catalysts, mainly as multiwall carbon nanotubes (MWCNTs) and bamboo carbon nanotubes. Fe-Mo catalysts showing best results in thermobalance were tested in a pilot-scale plant with a rotary bed reactor leading to high conversions of methane (70%) and formation of MWCNTs (8 g_{NC}/h).

* Corresponding author: (I.S.) Tel. +34976733977; Fax: +34 976733318; e-mail address: isuelves@icb.csic.es

Keywords: Hydrogen, Catalytic Decomposition of Methane, Fe Catalysts, Mo catalysts, bimetallic catalysts, multiwall carbon nanotubes, bamboo carbon nanotubes.

1. Introduction

Nanostructured carbon (NC) has attracted the attention of numerous researchers since the discovery of the carbon nanotubes (CNTs) by Iijima in 1991 [1]. CNT consist of one or more rolled graphene layers resulting in many tubular structures, differing in length, thickness, type of helicity and number of layers or walls, from single wall (SWCNTs) and double (DWCNTs) to multiwall carbon nanotubes (MWCNTs).

CNTs are typically produced by Chemical Vapor Deposition (CVD) from decomposition of various hydrocarbons (mainly CH_4 or C_2H_2) or CO using as catalysts transition metals supported on different metal oxides [2]. One interesting approach to the production of such carbon nanofilaments is the so-called catalytic decomposition of methane (CDM) [3, 4]. CDM is an endothermic reaction that produces in one single step free-CO_2 hydrogen and carbon nanostructures with various textural and structural properties [5]. Co- and Ni-based catalysts are widely used in CDM due to their high activity and the formation of filamentous carbon [6-11]. However, Ni and Co-based catalysts suffered from rapid deactivation when used at temperatures higher than ca. 650 ºC due to metal particle encapsulation by carbon [12-16]. Fe-based catalysts can operate at higher temperatures than Co or Ni based catalysts without suffering from deactivation, resulting in higher methane conversions due to the positive shift of the thermodynamic equilibrium. As an example, the equilibrium methane conversion at 650ºC is 71%, whereas at 800ºC increases up to 92%. Beside this, Fe based catalysts are cheaper and more environmental friendly than Co and Ni based catalysts.

Our group has recently synthesized high loaded iron oxide based catalysts with Al_2O_3 and MgO as textural promoters (Fe/MgO and Fe/Al_2O_3) [14, 15, 17, 18]. These catalysts showed methane conversion values close to equilibrium along with the production of MWCNTs and bamboo CNTs (also named as chain-like type [19]). Iron catalysts, however, exhibited lower catalytic activity than the nickel ones [7, 14, 20].

In order to improve Fe-based catalysts performance, several transition metals (Co, Ni, Mo, Pd, Mn and Cu) have been used as catalyst additives [6]. Bimetallic Fe-based catalysts such as Fe-Co [8, 21-23] or Fe-Mo [24-34] resulted in higher CNTs yield compared to undoped catalysts, besides preventing catalyst particle aggregation [35]. It is known that an increase in Mo content in bimetallic catalysts led to narrower nanotubes, i.e. less graphene layers, at the expense of carbon yield in the hydrocarbon decomposition process [27, 29, 30, 33, 34, 36].

Stable oxides (Al_2O_3, MgO, SiO_2, TiO_2, ZrO_2, etc.) are the supports most commonly used for NC formation by CDM in high-loaded metal catalysts [21, 37]. In Fe catalysts, the support acts like textural promoter affecting both the NC yields and the structure and morphology of the carbon nanofilaments produced [37].

In this work, massive Fe catalyst doped with different Mo loadings were prepared using either MgO or Al_2O_3 as textural promoters. CDM performance was evaluated firstly in a thermobalance in isothermal and ramp mode. Catalysts showing better performance were subsequently scaled up in a rotary bed reactor. NC quality, which is of utmost importance for its future application, has been determined by structural, textural and morphological characterization.

2. Experimental

2.1. Catalyst preparation

In order to study the NC formation in CDM reaction, the following Fe-based catalysts were prepared: Fe/Al_2O_3 (molar ratio: 2:1) and Fe/MgO (2:1), where Fe acts as active phase in the CDM process and Al_2O_3 and MgO as textural promoters. Fresh catalysts were synthesized by the fusion method from mixture of the respective salts and subsequent calcination in air at 450 °C during 2 hours [17]. The molar ratio of the components (2:1) was selected according to prior work conducted by our research group [15]. Catalysts were doped with Mo in different loadings: 2.5, 5, 7.5 and 10 % (molar, expressed as MoO_3). Catalysts are hereafter denoted as $FeMo(X)/Al_2O_3$ or FeMo(X)/MgO, where X refers to the MoO_3 amount in molar percentage. The fresh-catalyst powder were then grounded and sieved to select particles with sizes in 100−200 μm range.

2.2. Experimental configurations and CDM tests

The performance of the catalyst synthesized in the methane decomposition reaction was preliminarily studied in a thermobalance (CAHN TG-2151) at different operating temperatures. The evolution of the catalyst activity was recorded gravimetrically via the observed weight changes of the sample due to progressive carbon deposition as a reaction product of the CDM, as previously reported in [38]. Two temperatures modes were used: temperature programmed mode (using a heating rate of 10 ºC/min) from 400 ºC to 900 ºC and isothermal mode (at 700, 750 and 800 ºC) for 10 h. In a typical run, 10 mg of fresh catalyst was used and a methane flow rate of $1L_N$/min. Under these conditions, maximum carbon deposition and subsequent deactivation of the catalyst is assured [6, 36, 37]. Prior to CDM tests, fresh catalyst was reduced using a heating ramp

of 10 ºC/min from room temperature to 750 ºC with a H_2 flow rate of 1 L_N/h and then maintained at this temperature until complete reduction of catalyst.

A rotary bed reactor (RBR) set-up consisted of a cylindrical drum made of Kanthal rotating around its horizontal axis was used to evaluate at higher scale magnitude the best catalysts synthesized. The diameter and length of the cylinder were 0.065 and 0.80 m, respectively, and the rotational speed can be varied from 1 to 20 rpm. Additional details of the experimental apparatus can be found elsewhere [39]. Prior to CDM tests, fresh catalysts were subjected to a reduction treatment using a heating ramp of 10 ºC/min from room temperature to 750 ºC with a H_2 flow rate of 70 L_N/h and then maintained at this temperature for 1 h. Next, CDM reaction temperature was set at 750 °C. The feed consisted of pure methane (99.99%) adjusted to a weight hourly space velocity (WHSV, defined here as the methane flow rate at normal conditions per gram of catalyst initially loaded) of 1,5 $L_N/(h \cdot g_{cat})$. The composition of the outlet gas was determined by micro GC (Varian CP4900) equipped with two packed columns and a Thermal conductivity detector (TCD). The carbon produced was directly measured by weight difference, corresponding satisfactorily with the mass of carbon expected from the mass balance within an error of less than 5%. Methane conversion was calculated from the eq. (1), where $\%H_2$ is the H_2 content in the outlet gases expressed as a volume percentage.

$$\chi_{CH_4} = \frac{\%H_2}{200 - \%H_2} \qquad (1)$$

An estimation of carbon accumulated, g_C, during CDM reaction in RBR was determined from the methane conversion evolution by the equation:

$$g_C = \frac{M_C}{\alpha} \int_0^t \cdot F_{CH_4} \cdot \chi_{CH_4} \cdot dt \qquad (2)$$

where α is the standard molar volume, M_C is the atomic weight of carbon, F_{CH_4} is the methane flow rate fed to the reactor, and t is the total run time.

Carbon content is expressed as the carbon deposited with respect the amount of active phase in the catalysts: Fe or Fe + Mo (when Mo is present in the catalyst formulation).

2.3. Characterization techniques

The catalysts were characterized by X-ray diffraction (XRD) and temperature-programmed reduction (TPR), while the NC quality obtained in CDM tests was determined using structural (XRD), textural (N_2 adsorption) and morphology characterization (SEM and TEM).

XRD patterns of fresh catalysts and obtained NC were acquired in a Bruker D8 Advance Series 2 diffractometer. The angle range scanned was 10º-80º using a counting step of 0.05º and a counting time per step of 3 s. A suitable sample holder with a very low noise level was used, allowing for pattern acquisitions from a small amount of sample with high resolution. The powder XRD patterns were further processed using the accompanying DIFRAC PLUS EVA 8.0 to obtain refined structural parameters of crystal domain sizes of iron (metal, oxide or carbide) and deposited carbon through the application of Rietveld methods. The interlayer spacing, d_{002}, the mean crystallite size along c axis, *Lc*, and graphitization degree, *g*, are used in this study to assess the degree of structural order of the materials [40]. The mean interlayer spacing, d_{002}, was evaluated from the position of the (002) peak applying Bragg's equation [41]. The mean crystallite size, *Lc*, was calculated from the (002) peak using the Scherrer formula, with a values of K = 0.9 [41]. The graphitization degree, *g*, was calculated from the Mering and Maire equation (validity range: $0.3354 \leq d_{002} \leq 0.3440$ nm) [37, 42].

The reducibility of the fresh catalysts was studied by TPR. The respective reduction profiles were obtained in an AutoChem Analyzer II 2920 (Micromeritics) provided with a TCD from a sample amount of 10 mg and using a heat rate of 5 ºC/min within a

temperature range from room temperature to 1050 ºC under a flow rate of 50 ml/min of a H_2 (10%)/Ar mixture.

The textural properties of the deposited carbon were measured by N_2 adsorption at 77 K in a Micromeritics ASAP2020 apparatus. The specific surface areas and pore volumes were calculated by applying the BET method to the respective N_2 adsorption isotherms.

The morphological appearance of the deposited carbon was studied with a scanning electron microscope (Hitachi S-3400) coupled to a Si/Li detector for energy dispersive X-ray (EDX) analysis, and a transmission electron microscope (Tecnai F30), equipped with a cannon of 300 KeV, EDX / EELS analyzers and a maximum resolution of 1,5 Å.

3. Results and Discussion

3.1. Fresh catalysts characterization

XRD diffraction patterns of the fresh catalysts for different MoO_3 loading ranging from 0 to 10% and textural promoters, namely Al_2O_3 and MgO, are shown in Figure 1a and 1b, respectively. In both cases, undoped catalysts showed typical reflexions assigned to Fe_2O_3. Figure 1a did not show Al_2O_3 reflections, revealing its amorphous nature [36], whereas two reflexions were observed in Figure 1b assigned to MgO. Doping of the Al_2O_3 catalysts with Mo resulted in the disappearance of the Fe_2O_3 reflexions, regardless of the Mo loading, and the presence of very broad signals typically assigned to γ-Al_2O_3 can be distinguished [22]. The disappearance of Fe_2O_3 reflexions as a result of Mo addition may be attributed to a good dispersion of the Fe_2O_3 phase, since Mo promotes the formation of small metal particles [36, 43] with crystal domain size below the detection limit of the XRD technique. In catalysts prepared with MgO, diffractions assigned to MgO and Fe_2O_3 can be observed. A reduction in the crystallinity of Fe_2O_3 and MgO is also observed with increasing Mo content [27]. On further inspection,

catalysts doped with Mo amount higher than 5% showed weak reflexions around 20-35º (2θ) that could be assigned to MoO_3 most representative planes [44]. Furthermore, other species, formed upon interaction between Fe and/or Mo with textural promoters such as $MgFe_2O_4$, $MgFe_3O_4$, $FeMoO_4$, $Fe_2(MoO_4)_3$, $MgMoO_4$ and $MgMo_2O_7$ may be present in this narrow 2θ range, although the identification of these peaks is not straightforward [27, 29, 33]. These phases are originated in the calcination process by interaction between metal and promoter precursors; $MgFe_2O_4$ and $FeMoO_4$ were detected in a high temperature calcination (900 ºC) [33], where iron is well-dispersed in a $MgFe_2O_4$/MgO or $FeMoO_4$/MgO solid solution formed by the interdiffusion between FeOx and MgO [45]. $MgMoO_4$ is formed by interaction between Mo and MgO forming a solid solution [27, 29]. Fe_2O_3 and MoO_3 (or Mo like heterometaloxanes) may be well dispersed in small sizes in a low concentration in a solid solution in the support lattice [43].

Table 1 shows the Fe_2O_3 crystal domain size in the fresh catalyst obtained by XRD. Undoped catalysts prepared with Al_2O_3 had a crystal domain size of 17.7 nm, lower than the one prepared with MgO (24.5 nm). Mo effect on the Fe_2O_3 crystal domain size can be evaluated for the FeMo(X)/MgO catalyst. Thus, a gradual reduction in the Fe_2O_3 crystal domain size is observed as the MoO_3 content increased up to 7.5%. Thus, Fe_2O_3 crystal domain size was 24.5 nm for the undoped catalyst, whereas for FeMo(7.5)/Al_2O_3 catalysts was 18.4. However, further increase in MoO_3 loading provoked a slight increase in Fe_2O_3 crystal domain size. In all cases, crystal domain size is within the range 18.4-25.9 nm. Fe_2O_3 sizes below 30 nm promotes the formation of α-Fe and Fe_3C (cementite) during methane decomposition [19]. These species are catalytically active in the process allowing a gradual carbon accumulation during nanofilament growth. By contrast, larger Fe_2O_3 particles favor its transformation into non-catalytic γ-Fe saturated

with carbon atoms (austenite). For FeMo(X)/Al_2O_3 catalysts, Fe_2O_3 crystal domain size cannot be calculated due to the low crystalline nature of these samples.

The study of the reducibility of the fresh catalysts carried out by TPR is shown in Figure 2. The TPR profiles of FeMo(0)/Al_2O_3 catalysts showed the presence of three well differentiated reduction regions, indicating a stepwise reduction process. The first region was composed by a H_2 consumption peak centred at temperatures around 350 ºC, which reflected the first stage of the reduction of hematite, bulk principally [46], to magnetite: $Fe_2O_3 \rightarrow Fe_3O_4$. The second broad reduction peak found at temperatures between 420 and 750 ºC represented the reduction of magnetite to metallic iron: $Fe_3O_4 \rightarrow$ α-Fe. This intermediate temperature region is assigned to the two-step magnetite reduction sequence, $Fe_3O_4 \rightarrow FeO \rightarrow$ α-Fe [47]. The appearance of broad reduction region in the high temperature range (750-950 ºC) indicated the presence of different mixed oxides whose chemical nature and degree of crystallinity cannot be assessed surely. These species can be assigned to Fe (III) aluminates reduced in successive stages to form Fe (II) aluminates and α-Fe [46]. Mo addition induced significant changes in the Al_2O_3 catalysts TPR profiles. The peak in the first reduction region presented a similar shape as the undoped catalyst, although it was slightly shifted to higher temperatures. The H_2 consumption in the second region diminished dramatically. A new reduction peak appeared centred at ca. 750 ºC, being larger as the Mo content increased. Therefore, this peak is ascribable to the reduction of Mo species (MoO_3 or Mo ferrites) to an oxide with a lower chemical valence, that is, MoO_2, in accordance with literature data [48, 49]. The two peaks observed in the third region did not change as the Mo content increased.

The TPR profiles of the MgO catalysts showed two H_2 consumption regions: in the first region, between 300 ºC and 550 ºC, a shoulder and a peak centred at 350 and 470 ºC,

respectively, were observed. Both H_2 consumption regions can be assigned to the reduction of bulk Fe_2O_3 species with different interactions with MgO. The appearance of the shoulder can be attributed to the higher Fe content of the MgO catalysts as compared to the Al_2O_3 based catalysts. The second region between 500 ºC and 700 ºC was related to the stepwise reduction of Fe_3O_4 to FeO and Fe. No H_2 consumption in the high temperature domain was detected, which may imply that weaker interaction takes place between Fe and MgO, as compared to the Al_2O_3 based catalysts. Mo addition to MgO based catalysts shifted the peaks in both regions to higher temperatures. The intensity of the peak observed in the first reduction region diminished as the Mo content increased. The broad peak observed centered at ca. 750-800 ºC corresponded to the reduction of FeO and MoO_3 [48].

In both cases, Mo doping shifted the reduction peaks toward higher temperatures, indicating that it promoted a decrease in the reducibility of catalysts. This fact can be ascribed to a stronger metal particles and textural promoter interaction, probably due to the small size of metal particles, as indicated in the XRD discussion.

XRD of catalysts reduced at 750 ºC are shown in Figure 3 a and 3 b for the Al_2O_3 and MgO based catalysts, respectively. Al_2O_3 present typical reflections related to 110 and 200 planes of Fe [50], whereas MgO based catalysts presented a better developed cristallinity resulting in the appearance of Fe reflections assigned to 110 and 200 planes, and MgO assigned to 200 and 220 planes [51]. Fe crystal domain size in the reduced catalysts was calculated and the results are shown in Table 1. It is observed in all cases that the reduction of Fe_2O_3 to metallic Fe in the reduction pre-treatment affected the Fe crystal domain size by enlarging it, probably due to sintering upon the catalyst reduction stage. For instance, the Fe crystal domain size in the reduced catalysts is 89.7 and 50.2

nm for the FeMo(0)/Al_2O_3 and FeMo(10)Al_2O_3, respectively. Fe crystal domain size in FeMo(X)/Al_2O_3 catalysts is lower than in FeMo(X)/MgO catalyst. An increase in Mo loading had no effect in the Fe crystal domain size of the Al_2O_3 based catalysts, whereas it promoted a decrease of the Fe domain size in the MgO based catalysts. Regarding Mo content, the trend in Fe crystal sizes was similar to that of Fe_2O_3 in fresh catalysts. Mo presence is known to form heteropolymolybdates or ferrites type structures in fresh catalyst which favor formation and stabilization of metallic particles of smaller size in the reduction step. It also hinders the sintering of the active nanosize metal clusters into coarse poorly active particles [43].

3.2. Thermogravimetric analysis of Fe-based catalysts

3.2.1. Temperature-ramp tests

As previously commented, CDM reaction was studied by monitoring the mass gained as the temperature was increased from 500 ºC to 900 ºC with a heating rate of 10 ºC·min^{-1}. TGA results obtained with Fe and FeMo catalysts prepared with Al_2O_3 and MgO as textural promoters are shown in Figures 4a and 4b, respectively. Insets in Figure 4 show the carbon formation rate (CFR) for the catalyst prepared with Al_2O_3 and MgO as textural promoter, respectively, calculated from the numerical derivative of the carbon content *vs.* time curves.

For both textural promoters used, Mo addition improved catalyst performance as compared to the undoped catalysts, as previously reported [27, 29, 30, 33, 34, 36]. This fact can be confirmed attending to the higher amount of carbon accumulated (Figures 4 a and 4 b) and the higher CFR in the ramp tests (insets). This improvement in catalyst performance was observed up to a certain amount of MoO_3 loading. Thus, maximum

carbon accumulation capacity was found to be 5% and 7.5% for the catalysts prepared with Al_2O_3 and MgO, respectively. Comparing with other results in literature, MoO_3 optimum loading in Al_2O_3 supported catalysts varies from 5.8% (mol) in a 52% (wt.) Fe_2O_3 content catalyst [36] to 12% (mol) in very low Fe loaded catalyst (3.5 wt.%) [34]. Similarly, CFR was higher for catalyst prepared with 7.5% Mo loading for the case of MgO catalyst, whereas optimum results were obtained for catalyst prepared with 5 and 7.5% when Al_2O_3 was used as textural promoter. The evaluation of the textural promoter used revealed that better results, both in terms of carbon accumulation capacity and CFR, were obtained for catalysts prepared with Al_2O_3.

Ramp temperature tests can also provide valuable information about the optimum window temperature to carry out the CDM avoiding catalyst deactivation, highlighting the differences upon the textural promoter used.

CFR curves of Al_2O_3 catalysts show almost negligible values up to temperatures of 650 ºC, and from this temperature and onwards, a sharp increase in the CFR was observed. The curves ended with a dramatic decrease of CFR, possibly due to catalyst deactivation at high temperature. CFR curves obtained with MgO catalysts revealed a different shape. CFR was very low at temperatures lower than 700ºC. A sharp increment occurred at 700-750º, followed by a progressive increment up to a maximum (850ºC) and then a progressive deactivation. In this case, by the time that the ramp ended, the catalysts maintained a relative high CFR, therefore total deactivation was not attained during the course of these tests. For Mo doped catalyst, a constant CFR temperature range appeared. Thus, Mo doped Al_2O_3 based catalysts had a temperature window in which CFR was maximum between ca. 700-850 ºC, whereas Mo-doped MgO catalysts this window is shifted to higher temperatures, between 750 and 900ºC.

It can be concluded that Mo addition improved catalyst performed in the catalysts prepared with Al_2O_3 and MgO as textural promoter. Catalyst prepared with Al_2O_3 yielded higher carbon accumulation capacities and carbon formation rates than MgO catalyst in the tests carried out in isothermal tests. These results can be tentatively explained according to the characterization results presented in Section 3.1. Thus, maximum carbon accumulation was obtained for catalysts with smallest Fe crystal domain size (Table 1), related to a stronger metal-promoter interaction, as discussed in section 3.1.

Taking into account both carbon accumulation capacities and CFR, optimum Mo loading was in the range 2.5-7.5% for Al_2O_3 catalysts, whereas for MgO based catalyst an optimum at 7.5 % Mo loading was obtained. Catalysts with 7.5% Mo content prepared with both textural promoters were selected for next studies carried out at isothermal conditions.

3.2.2. Isothermal tests

CDM was carried out in isothermal mode at three different temperatures, namely 700, 750 and 800 ºC. Figure 5 shows the carbon accumulated with time for FeMo(0)/Al_2O_3 (Figure 5a), FeMo(0)/MgO (Figure 5b), FeMo(7.5)/Al_2O_3 (Figure 5c) and FeMo(7.5)/MgO (Figure 5d) catalysts. Runs were carried out until the mass gain was almost negligible.

In both cases, Mo addition improved significantly the catalyst performance, indicated by the higher ultimate carbon accumulation, (UCA), i.e., the amount of carbon accumulated until deactivation occurred. It was observed that temperature did not affect catalyst performance on non-doped catalysts, whereas it had a great impact on the Mo doped catalysts. For both catalyst tested, tests carried out a 700 ºC resulted in a relative

slow initial carbon deposition rate, as revealed the curve slopes. At 800 ºC, TGA curves were characterized by a sharp increase in the amount of carbon accumulated in the initial stage of the reaction followed by a rapid deactivation after ca. 50-100 min time on stream (TOS). Catalyst performance at 750 ºC presented an intermediate behaviour, achieving larger value of UCA for both catalysts. Therefore, it can be concluded that optimum operation temperature for these catalysts in the CDM reaction is 750ºC. It is known that temperatures above 680 ºC guarantee the Fe_3C transformation into its metastable state and the formation of the α-Fe phase in a considerable amount, the latter being active to CDM [37].

Isothermal tests revealed that the UCA obtained for the catalyst doped with 7.5% Mo was slightly larger for Al_2O_3 based catalysts, although the main impact on the textural promoter used was observed in the time needed to reach this value. This implies that catalyst prepared with Al_2O_3 had higher kinetics in the CDM reaction.

At isothermal conditions, CFR decreased dramatically with time, as deducted from the curve slopes. This indicates that a large fraction of the carbon accumulated is obtained during the initial stage of the runs. UCA values obtained at 750 ºC with FeMo(7.5)/Al_2O_3 and FeMo(7.5)/MgO were 13.4 and 12.4 g_C/g_{Fe}, respectively. Comparing the UCA values of this work with others Fe-Mo catalysts employed in literature for CNTs synthesis, large differences depending on WHSV, reaction temperature, pressure, feed or Fe/Mo ratio in the catalyst were observed, therefore the comparison is not straightforward. As an example, UCA values ranging from 8.6 to 46.2 g_C/g_{Fe} for Fe-Mo catalysts were reported [29, 34].

3.3. Characterization of spent catalysts

Figure 6 shows the diffractograms of the catalysts after isothermal tests at 750 ºC. In all cases, besides the Fe reflection at ca. 44.9º of Fe (110), new reflections as compared to the fresh reduced catalysts appeared: a prominent reflection at ca. 26º, assigned to the 002 plane of the graphitic structure of deposited carbon, several reflections identified as Fe_3C and the presence of Mo_2C at ca. 39.9º. Rietvel analysis revealed some distinct features in the crystal domain size of Fe and Fe_3C on the spent catalysts, as shown in Table 2. Thus, Fe crystal domain size diminished in all cases as compared to the fresh reduced catalysts. This can be attributed to a fragmentation of Fe particles after the initial stage of carbon filaments formation [37].

Fe_3C crystal domain size on the spent catalysts tested at 750 ºC varied considerably as a function of the textural promoter used. Thus, MgO based catalysts had a relative large Fe_3C crystals (ca. 40 nm), and Mo addition had no impact. On the other hand, Al_2O_3 catalysts showed smaller Fe_3C crystals as compared to MgO catalysts. Additionally, it was observed that Mo addition led to Mo_2C formation, which prevents the enlargement of Fe_3C crystal and improve the dispersion and catalytic activity of Fe [43]. Thus, Fe_3C crystal domain size was 21.5 and 12.6 nm in the spent $FeMo(0)/Al_2O_3$ and $FeMo(7.5)/Al_2O_3$, respectively. Mo addition avoids the crystallization of Fe_3C inhibiting the catalytic activity of metal due to the slower diffusion of carbon in Fe_3C, compared with solutions of carbon in α-Fe [43, 52].

It is known that the eutectic mixture of Mo and Fe, and their carbides, has a lower melting point which would favor the diffusion of dissolved carbon during formation of carbon nanofilaments [43]. The presence of Fe_3C, Mo_2C and active Fe particles in the spent catalysts, as shown in Figure 6, supports the carbide cycle mechanism [37]: Fe_3C is formed by methane decomposition on the free surface fragment of the catalytic particle. Since Fe_3C is metastable under certain conditions, it is decomposed to form

graphitized carbon in form of filamentous carbon and α-Fe, the latter being active to hydrocarbons decomposition. Thus, the presence of α-Fe and Fe_3C in the catalytic particle is necessary for oriented carbon growth. Finally, deactivation may be due to the fragmentary dispersion of Fe particles, which is accompanied by encapsulation of residual particles by growing carbon nanofilament. This fact is in agreement with a reduction Fe crystal size as compared to the reduced catalysts shown in Table 2, as discussed above.

SEM study shown in Figure 7 provides more insight about the morphological differences of the carbon deposited on the different catalysts used, which clearly appeared as nanofilaments emerging from Fe-Mo particles. Al_2O_3 catalysts (Figures 7a and 7b) led to more homogeneous filaments and higher aspect ratio than those produced with MgO catalysts (Figures 7c and 7d). Mo doping affects the final appearance of the NC depending on the textural promoter: Al_2O_3 spent catalysts exhibited no significant topographic differences influenced by Mo doping (Figure 7b), whereas MgO Mo-doped catalysts improved the formation of carbon nanofilaments with a higher aspect ratio (Figure 7d).

Product quality is determined as a function of textural and structural parameters of NC. Surface area of products (NC + catalyst) depends on the extent of CDM reaction as seen in Table 2. Mo addition enhanced carbon formation resulting in a spent catalyst with larger surface area values (118-123 m^2/g for FeMo(7.5)/Al_2O_3 and FeMo(7.5)/MgO, respectively), than the analogous spent undoped catalysts (82-35 m^2/g), larger pore volumes and lower pore sizes. The high graphitic nature of nanofilaments is reflected by the structural parameter of graphitic carbon (see Table 2) such as the graphitization degree, g, the interplanar distance, d_{002}, or crystallite size, L_c, which are close to those of graphite.

3.4. Scaling-up in a rotary bed reactor installation

In this section, the scaling up of the CDM using the Mo doped catalysts selected in previous section was carried out using a RBR. This set up has been previously used as an alternative to other types of moving bed reactors (fluidized bed) and to study of Fe- and Ni-based catalysts in CDM [14, 39]). Figure 8 shows conversion and carbon accumulation data for FeMo(7.5)/Al_2O_3 and FeMo(7.5)/MgO catalysts tested in 180 min duration tests in the RBR at 750ºC and a WHSV of 1.5 $_{N}l \cdot g_{Cat}^{-1} \cdot h^{-1}$. Methane conversion and carbon accumulated were calculated from eq. 1 and eq. 2, respectively.

Al_2O_3 yielded higher CH_4 conversion during the course of the tests, as compare to the MgO catalysts, with initial CH_4 conversions of 75 and 69%, respectively. Both catalysts suffered from slight deactivation as the TOS increased. This deactivation was more dramatic for the catalysts prepared with MgO as textural promoter. Comparing the carbon accumulated during the TOS (180 min) at both experimental set-ups (thermobalance and RBR), same trends in terms of carbon accumulation capacity were observed. Thus, after 180 min TOS, the amount of carbon accumulated in RBR was 2.88 and 1.64 and g_{CN}/g_{Fe+Mo} for FeMo(7.5)/Al_2O_3 and FeMo(7.5)/MgO, respectively. On the other hand, TB obtained 7.73 and 5.73 g_{CN}/g_{Fe+Mo} (on 180 min), respectively. Therefore, TB at isothermal mode represents a valuable tool for rapid testing of catalysts, although RBR is needed in order to obtain larger NC productions. However, the ultimate mass gained per gram of metal (Fe + Mo) by these catalysts is lower due to less forced operation: TB works at much higher WHSV to exhaust catalyst activity until its deactivation as compared to RBR.

3.4.1. Nanostructured carbon characterization

Some TEM micrographs of the NCs produced in RBR by CDM are shown in Figures 9 (spent FeMo(7.5)/Al_2O_3) and Figure 10 (FeMo(7.5)/MgO). In Figures 9a and 10a are shown some representative overviews of spent catalysts, revealing certain heterogeneity in diameters and the presence of nanofilaments of several sizes and structures, mainly carbon nanotubes. Spent FeMo(7.5)/Al_2O_3 showed tubular structures with a relative narrow diameter distribution (Figure 9a and 9b), while spent FeMo(7.5)/MgO presented a wider diameter distribution (Figure 10a) showing some tubular structures up to 100 nm in diameter grown from coarse particles (Figure 10b). Both samples showed coarse catalyst particles with deposits of carbon and, probably, inactive crystalline Fe_3C [52].

Carbon nanofilaments are formed from Fe crystals of different sizes, resulting in different graphitic carbon structures. In Figures 9b and 9c, and Figures 10c and 10d several metal particles can be observed, varying in size (from 10 to 60 nm) and morphology, with common characteristics as enlarged and rounded appearance. Graphene parallel planes are generated from carbon diffusion through Fe-Mo particles to the longitudinal sides, thereof emerging different carbon nanofilaments. This process occurs until eventual catalyst deactivation once metal particles are fully covered by carbon and as a result of catalyst particles segregation (Figure 10c) [15, 37].

As discussed, CNTs production consist of bamboo CNTs (Figures 9b and 9c and Figures 10b and 10c), nanotubes with a few layers, known as thin multiwalled carbon nanotubes (t-MWCNTs) (Figure 9d), and MWCNTs of 10-20 nm in diameter (Figure 10d). These carbon nanostructures are characterized by the parallel arrangement of graphene layers to nanotube axis forming a continuous hollow core (5-10 nm); except for the bamboo type that presented internal nodes that disrupt the hollow core. Bamboo nanotubes appeared after the segregation of catalytic particles evidencing the high fluidity of Fe particles during carbon nanofilaments growth. Metal particle segregation

accounts for the formation of bamboo nanotubes [37]. Regarding carbon quality, structural and textural parameters were similar to carbons obtained in TB, characterized by having high graphitic order and slightly low surface areas.

4. Conclusions

On the basis of the results described above, we concluded as follows:

- Ramp mode thermobalance was stated as a reliable tool for rapid catalysts screening in the CDM reaction. Catalyst performances were evaluated in carbon formation terms where optimum catalyst formulation and its operation temperature range can be easily determined.
- Carbon formation by CDM started from 500 ºC and accelerate between 650 and 700 °C for iron catalysts due to the formation of metastable Fe_3C, resulting in carbon growth. Maximum CFRs were obtained at temperatures in the range of 700-900 °C depending on textural promoter used.
- Mo addition enhanced carbon formation showing different optimum contents depending on the catalyst promoter used. This was attributed to a different metal/support interaction, as TPR study revealed. Mo doping favored the dispersion of small Fe_2O_3 particles in the fresh catalyst, which in subsequent stages of reduction and CDM reaction were converted to Fe and Fe_3C, favoring the carbon diffusion into the catalyst particle during the carbon nanofilament growth.
- Fe-Mo catalysts formed carbon nanofilaments, mainly MWCNTs and bamboo nanotubes with high grade of graphitization and interesting textural properties. During CDM, the fragmentation of the active metal particles took place leading to bamboo structures and the deactivation by encapsulation. Morphological

differences as a function of the textural promoters used resulted in different diameter distribution in tubular carbon nanostructures.

- A pilot-scale plant with a rotary bed reactor is shown as an efficient and scalable set-up for free-CO_2 hydrogen production and carbon nanofilaments, obtaining high methane conversions (70%) and formation of MWCNTs (8 g_{NC}/h).

Acknowledgments

Work partially supported by FEDER and the Spanish Science and Innovation Ministry (ENE2008-06516-C03-01) and by the Spanish Economy and Competitiveness Ministry (ENE2011-28318-C03-01).

References

[1] Iijima S. Helical microtubules of graphitic carbon. Nature. 1991;354:56-8.
[2] Kumar M, Ando Y. Chemical vapor deposition of carbon nanotubes: A review on growth mechanism and mass production. Journal of Nanoscience and Nanotechnology. 2010;10:3739-58.
[3] Muradov N. Hydrogen via methane decomposition: An application for decarbonization of fossil fuels. International Journal of Hydrogen Energy. 2001;26:1165-75.
[4] Abbas HF, Wan Daud WMA. Hydrogen production by methane decomposition: A review. International Journal of Hydrogen Energy. 2010;35:1160-90.
[5] Muradov N, Vezirolu T. From hydrocarbon to hydrogen?carbon to hydrogen economy. International Journal of Hydrogen Energy. 2005;30:225-37.
[6] Li Y, Li D, Wang G. Methane decomposition to COx-free hydrogen and nano-carbon material on group 8-10 base metal catalysts: A review. Catalysis Today. 2011;162:1-48.
[7] Ermakova MA, Ermakov DY. Ni/SiO2 and Fe/SiO2 catalysts for production of hydrogen and filamentous carbon via methane decomposition. Catalysis Today. 2002;77:225-35.
[8] Reshetenko TV, Avdeeva LB, Ushakov VA, Moroz EM, Shmakov AN, Kriventsov VV, et al. Coprecipitated iron-containing catalysts (Fe-Al2O3, Fe-Co-Al2O3, Fe-Ni-Al2O3) for methane decomposition at moderate temperatures: Part II. Evolution of the catalysts in reaction. Applied Catalysis A: General. 2004;270:87-99.
[9] Ichi-oka Ha, Higashi No, Yamada Y, Miyake T, Suzuki T. Carbon nanotube and nanofiber syntheses by the decomposition of methane on group 8-10 metal-loaded MgO catalysts. Diamond and Related Materials. 2007;16:1121-5.

[10] Avdeeva LB, Kochubey DI, Shaikhutdinov SK. Cobalt catalysts of methane decomposition: Accumulation of the filamentous carbon. Applied Catalysis A: General. 1999;177:43-51.
[11] Takenaka S, Kobayashi S, Ogihara H, Otsuka K. Ni/SiO2 catalyst effective for methane decomposition into hydrogen and carbon nanofiber. Journal of Catalysis. 2003;217:79-87.
[12] Ahmed S, Aitani A, Rahman F, Al-Dawood A, Al-Muhaish F. Decomposition of hydrocarbons to hydrogen and carbon. Applied Catalysis A: General. 2009;359:1-24.
[13] Konieczny A, Mondal K, Wiltowski T, Dydo P. Catalyst development for thermocatalytic decomposition of methane to hydrogen. International Journal of Hydrogen Energy. 2008;33:264-72.
[14] Pinilla JL, Utrilla R, Lázaro MJ, Moliner R, Suelves I, García AB. Ni- and Fe-based catalysts for hydrogen and carbon nanofilament production by catalytic decomposition of methane in a rotary bed reactor. Fuel Processing Technology. 2011;92:1480-8.
[15] Pinilla JL, Utrilla R, Karn RK, Suelves I, Lázaro MJ, Moliner R, et al. High temperature iron-based catalysts for hydrogen and nanostructured carbon production by methane decomposition. International Journal of Hydrogen Energy. 2011;36:7832-43.
[16] Cunha AF, Órfão JJM, Figueiredo JL. Methane decomposition on Ni-Cu alloyed Raney-type catalysts. International Journal of Hydrogen Energy. 2009;34:4763-72.
[17] Suelves I, Pinilla JL, Utrilla R, Lazaro MJ, Moliner R, Palacios JM. Catalizadores de hierro para la producción simultánea de hidrógeno y nanofilamentos de carbono mediante descomposición catalítica de metano.
[18] Torres D, de Llobet S, Pinilla JL, Lázaro MJ, Suelves I, Moliner R. Hydrogen production by catalytic decomposition of methane using a Fe-based catalyst in a fluidized bed reactor. Journal of Natural Gas Chemistry. 2012;21:367-73.
[19] Takenaka S, Serizawa M, Otsuka K. Formation of filamentous carbons over supported Fe catalysts through methane decomposition. Journal of Catalysis. 2004;222:520-31.
[20] Martin-Gullon I, Vera J, Conesa JA, González JL, Merino C. Differences between carbon nanofibers produced using Fe and Ni catalysts in a floating catalyst reactor. Carbon. 2006;44:1572-80.
[21] Avdeeva LB, Reshetenko TV, Ismagilov ZR, Likholobov VA. Iron-containing catalysts of methane decomposition: Accumulation of filamentous carbon. Applied Catalysis A: General. 2002;228:53-63.
[22] Tran KY, Heinrichs B, Colomer JF, Pirard JP, Lambert S. Carbon nanotubes synthesis by the ethylene chemical catalytic vapour deposition (CCVD) process on Fe, Co, and Fe-Co/Al2O3 sol-gel catalysts. Applied Catalysis A: General. 2007;318:63-9.
[23] MacCallini E, Tsoufis T, Policicchio A, La Rosa S, Caruso T, Chiarello G, et al. A spectro-microscopic investigation of Fe-Co bimetallic catalysts supported on MgO for the production of thin carbon nanotubes. Carbon. 2010;48:3434-45.
[24] Jeong HJ, Kim KK, Jeong SY, Park MH, Yang CW, Lee YH. High-yield catalytic synthesis of thin multiwalled carbon nanotubes. Journal of Physical Chemistry B. 2004;108:17695-8.
[25] Labunov VA, Basaev AS, Shulitski BG, Shaman YP, Komissarov I, Prudnikava AL, et al. Growth of few-wall carbon nanotubes with narrow diameter distribution over fe-mo-mgo catalyst by methane/acetylene catalytic decomposition. Nanoscale Research Letters. 2012;7:1-20.

[26] Li Y, Liu J, Wang Y, Zhong Lin W. Preparation of monodispersed Fe-Mo nanoparticles as the catalyst for CVD synthesis of carbon nanotubes. Chemistry of Materials. 2001;13:1008-14.
[27] Xu X, Huang S, Yang Z, Zou C, Jiang J, Shang Z. Controllable synthesis of carbon nanotubes by changing the Mo content in bimetallic Fe-Mo/MgO catalyst. Materials Chemistry and Physics. 2011;127:379-84.
[28] Xiong GY, Suda Y, Wang DZ, Huang JY, Ren ZF. Effect of temperature, pressure, and gas ratio of methane to hydrogen on the synthesis of double-walled carbon nanotubes by chemical vapour deposition. Nanotechnology. 2005;16:532-5.
[29] Dubey P, Choi SK, Kim B, Lee CJ. Synthesis of thin-multiwalled carbon nanotubes by Fe-Mo/MgO catalyst using sol-gel method. Carbon Letters. 2012;13:99-108.
[30] Shah N, Panjala D, Huffman GP. Hydrogen production by catalytic decomposition of methane. Energy and Fuels. 2001;15:1528-34.
[31] Shah N, Pattanaik S, Huggins FE, Panjala D, Huffman GP. XAFS and Mössbauer spectroscopy characterization of supported binary catalysts for nonoxidative dehydrogenation of methane. Fuel Processing Technology. 2003;83:163-73.
[32] Punnoose A, Shah N, Huffman GP, Seehra MS. X-ray diffraction and electron magnetic resonance studies of M/Fe/Al2O3 (M=Ni, Mo and Pd) catalysts for CH4 to H2 conversion. Fuel Processing Technology. 2003;83:263-73.
[33] Wen Q, Qian W, Wei F. Synthesis of Single-Walled Carbon Nanotubes with Narrow Diameter Distribution by Calcination of a Mo-Modified Fe/MgO Catalyst. Chinese Journal of Catalysis. 2008;29:617-23.
[34] Lamouroux E, Serp P, Kihn Y, Kalck P. Identification of key parameters for the selective growth of single or double wall carbon nanotubes on FeMo/Al2O3 CVD catalysts. Applied Catalysis A: General. 2007;323:162-73.
[35] Tang S, Zhong Z, Xiong Z, Sun L, Liu L, Lin J, et al. Controlled growth of single-walled carbon nanotubes by catalytic decomposition of CH4 over Mo/Co/MgO catalysts. Chemical Physics Letters. 2001;350:19-26.
[36] Chesnokov VV, Zaikovskii VI, Chichkan AS, Buyanov RA. The role of molybdenum in Fe–Mo–Al2O3 catalyst for synthesis of multiwalled carbon nanotubes from butadiene-1,3. Applied Catalysis A: General. 2009;363:86-92.
[37] Ermakova M. Decomposition of Methane over Iron Catalysts at the Range of Moderate Temperatures: The Influence of Structure of the Catalytic Systems and the Reaction Conditions on the Yield of Carbon and Morphology of Carbon Filaments. Journal of Catalysis. 2001;201:183-97.
[38] Pinilla JL, Suelves I, Lázaro MJ, Moliner R, Palacios JM. Activity of NiCuAl catalyst in methane decomposition studied using a thermobalance and the structural changes in the Ni and the deposited carbon. International Journal of Hydrogen Energy. 2008;33:2515-24.
[39] Pinilla JL, Utrilla R, Lázaro MJ, Suelves I, Moliner R, Palacios JM. A novel rotary reactor configuration for simultaneous production of hydrogen and carbon nanofibers. International Journal of Hydrogen Energy. 2009;34:8016-22.
[40] Cuesta A, Dhamelincourt P, Laureyns J, Martinez-Alonso A, M. D. Tascon J. Comparative performance of X-ray diffraction and Raman microprobe techniques for the study of carbon materials. Journal of Materials Chemistry. 1998;8:2875-9.
[41] Biscoe J. An X-Ray Study of Carbon Black. Journal of Applied Physics. 1942;13:364.

[42] Maire J, Mering J. Graphitization of Soft Carbons. Chemistry and Physics of Carbon. 1970;6:125-89.
[43] Melezhik AV, Romantsova IV, D'Yachkova TP, Bychkov ON, Shlykova AA, Smykov MA, et al. Effect of the matrix composition on the activity of metal oxide catalysts in CVD synthesis of carbon nanotubes. Russian Journal of Applied Chemistry. 2012;85:782-7.
[44] Sitepu H. Texture and structural refinement using neutron diffraction data from molybdite (MoO3) and calcite (CaCO3) powders and a Ni-rich Ni50.7 Ti49.30 alloy. Powder Diffraction. 2009;24:315-26.
[45] Ago H, Nakamura K, Uehara N, Tsuji M. Roles of metal-support interaction in growth of single- and double-walled carbon nanotubes studied with diameter-controlled iron particles supported on MgO. Journal of Physical Chemistry B. 2004;108:18908-15.
[46] Ren-Yuan T, Su Z, Chengyu W, Dongbai L, Liwu L. An in situ combined temperature-programmed reduction-Mössbauer spectroscopy of alumina-supported iron catalysts. Journal of Catalysis. 1987;106:440-8.
[47] Jozwiak WK, Kaczmarek E, Maniecki TP, Ignaczak W, Maniukiewicz W. Reduction behavior of iron oxides in hydrogen and carbon monoxide atmospheres. Applied Catalysis A: General. 2007;326:17-27.
[48] Kumar M, Aberuagba F, Gupta JK, Rawat KS, Sharma LD, Murali Dhar G. Temperature-programmed reduction and acidic properties of molybdenum supported on MgO-Al2O3 and their correlation with catalytic activity. Journal of Molecular Catalysis A: Chemical. 2004;213:217-23.
[49] Feng L, Li X, Dadyburjor DB, Kugler EL. A temperature-programmed-reduction study on alkali-promoted, carbon-supported molybdenum catalysts. Journal of Catalysis. 2000;190:1-13.
[50] Fjellvag H, Hauback BC, Vogt T, Stolen S. Monoclinic nearly stoichiometric wüstite at low temperatures. American Mineralogist. 2002;87:347-9.
[51] Hazen RM. Effects of temperature and pressure on the cell dimension and X-ray temperature factors of periclase. American Mineralogist. 1976;61:266-71.
[52] Mordkovich VZ, Dolgova EA, Karaeva AR, Kharitonov DN, Maslov IA, Kamenev AA, et al. Synthesis of carbon nanotubes by catalytic conversion of methane: Competition between active components of catalyst. Carbon. 2007;45:62-9.

Table 1. Crystal sizes of Fe_2O_3 and Fe of the fresh and reduced catalysts, respectively.

Catalyst	Fe_2O_3 crystal size (nm)	Fe crystal size (nm)
FeMo(0)/Al_2O_3	17.7	34.2
FeMo(2.5)/Al_2O_3	-	18.7
FeMo(5)/Al_2O_3	-	18.5
FeMo(7.5)/Al_2O_3	-	20.1
FeMo(10)/Al_2O_3	-	19.2
FeMo(0)/MgO	24.5	89.7
FeMo(2.5)/MgO	25.9	65.8
FeMo(5)/MgO	23.3	58.0
FeMo(7.5)/MgO	18.4	54.6
FeMo(10)/MgO	21.0	50.2

Table 2. Properties of spent catalysts after isotherm CDM tests at 750 ºC. Textural parameters determined by N_2 adsorption: BET surface area (S_{BET}), pore volume (V_P) and average pore size. Structural parameters determined by XRD for graphite (interplanar distance (d_{002}), crystallite size (L_c) and graphitization degree (g)) and Fe and Fe_3C (crystal size).

Catalyst	Textural Properties			Structural Properties				
	S_{BET} (m^2/g)	V_P (cm^3/g)	Pore size (Å)	d_{002} (nm)	g (%)	L_c (nm)	Fe (nm)	Fe_3C (nm)
FeMo(0)/Al_2O_3	82	0.29	143.2	0.3385	64	7.2	30.0	21.5
FeMo(7.5)/Al_2O_3	118	0.31	105.4	0.3373	78	5.3	19.2	12.6
FeMo(0)/MgO	35	0.15	169.1	0.3362	91	11.3	82.0	42.0
FeMo(7.5)/MgO	123	0.42	135.4	0.3372	79	6.0	33.9	39.2

FIGURE CAPTIONS

Figure 1. Powder XRD patterns of fresh calcined catalysts: a) FeMo(X)/Al_2O_3; b) FeMo(X)/MgO.

Figure 2. TPR profiles of the fresh calcined catalysts: a) FeMo(X)/Al_2O_3; b) FeMo(X)/MgO.

Figure 3. Powder XRD patterns of fresh reduced catalysts: a) FeMo(X)/Al_2O_3; b) FeMo(X)/MgO.

Figure 4. Evolution of carbon accumulated for catalysts during thermobalance ramp-mode CDM tests. Insets: evolution of the carbon formation rate with time: CFR ($g_C \cdot g_{Fe+Mo}^{-1} \cdot s^{-1}$) *vs* temperature (ºC). a) FeMo(X)/Al_2O_3; b) FeMo(X)/MgO.

Figure 5. Evolution of carbon accumulated with time at different reaction temperatures for catalysts: a) FeMo(0)/Al_2O_3; b) FeMo(0)/MgO; c) FeMo(7.5)/Al_2O_3; d) FeMo(7.5)/MgO.

Figure 6. Powder XRD patterns of spent catalysts after isothermal test carried out in thermobalance at 750 ºC: a) FeMo(0)/MgO; b) FeMo(7.5)/MgO; c) FeMo(0)/Al_2O_3; d) FeMo(7.5)/Al_2O_3.

Figure 7. SEM micrographs of spent catalysts after isothermal test carried out in thermobalance at 750 ºC for catalysts: a) FeMo(0)/Al_2O_3; b) FeMo(7.5)/Al_2O_3; c) FeMo(0)/MgO; d) FeMo(7.5)/MgO.

Figure 8. Methane conversion (closed symbols, left axis) and carbon formation per gram of metal (Fe + Mo) (open symbols, right axis). CDM reaction performed in RBR, T: 750 °C and WHSV: 1.5 $_N l \cdot g_{Cat}^{-1} \cdot h^{-1}$.

Figure 9. TEM micrographs of spent FeMo(7.5)/Al_2O_3 catalysts after tests carried out in RBR, T: 750 °C and WHSV: 1.5 $_N l \cdot g_{Cat}^{-1} \cdot h^{-1}$.

Figure 10. TEM micrographs of spent FeMo(7.5)/MgO catalysts after tests carried out in RBR, T: 750 °C and WHSV: 1.5 $_N l \cdot g_{Cat}^{-1} \cdot h^{-1}$.

Figure 1.

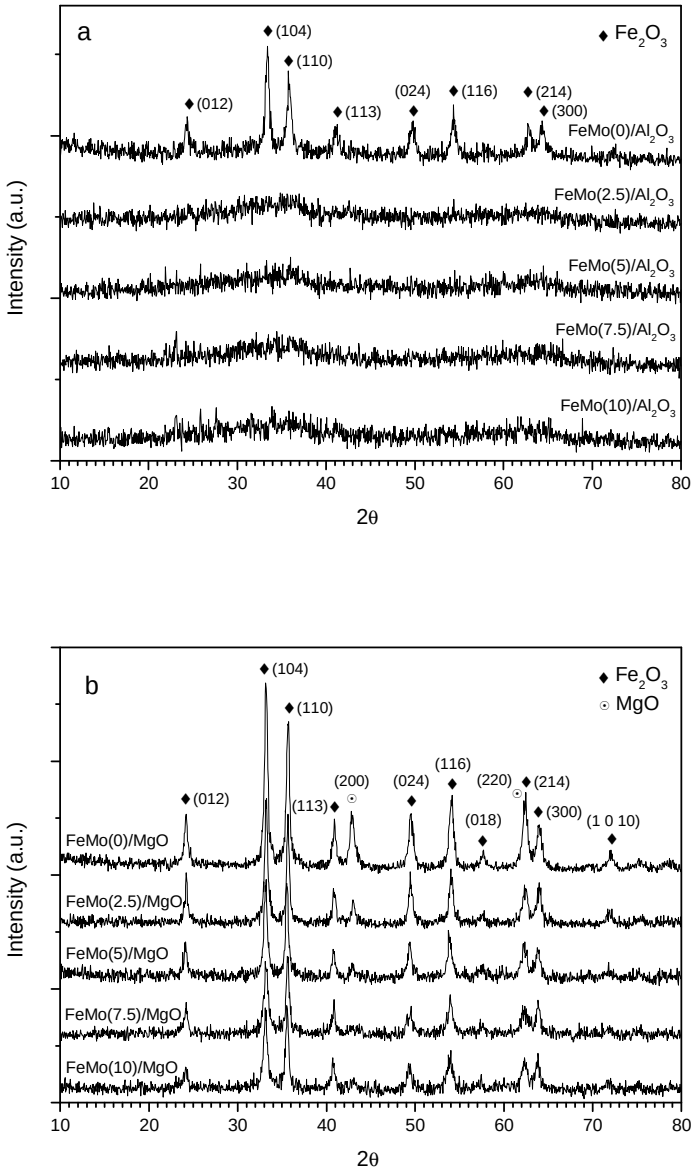
a
♦ Fe2O3
♦(104)
♦(110)
♦(012)
♦(113)
(024) ♦
♦(116)
♦(214)
♦(300)
FeMo(0)/Al2O3
FeMo(2.5)/Al2O3
FeMo(5)/Al2O3
FeMo(7.5)/Al2O3
FeMo(10)/Al2O3
Intensity (a.u.)
10 20 30 40 50 60 70 80
2θ
b
♦ Fe2O3
⊙ MgO
♦(104)
♦(110)
♦(012)
♦(113)
(200) ⊙
(024) ♦
(116) ♦
(220) ⊙
♦(214)
♦(300)
(018) ♦
(1 0 10) ♦
FeMo(0)/MgO
FeMo(2.5)/MgO
FeMo(5)/MgO
FeMo(7.5)/MgO
FeMo(10)/MgO
Intensity (a.u.)
10 20 30 40 50 60 70 80
2θ

Figure 2.

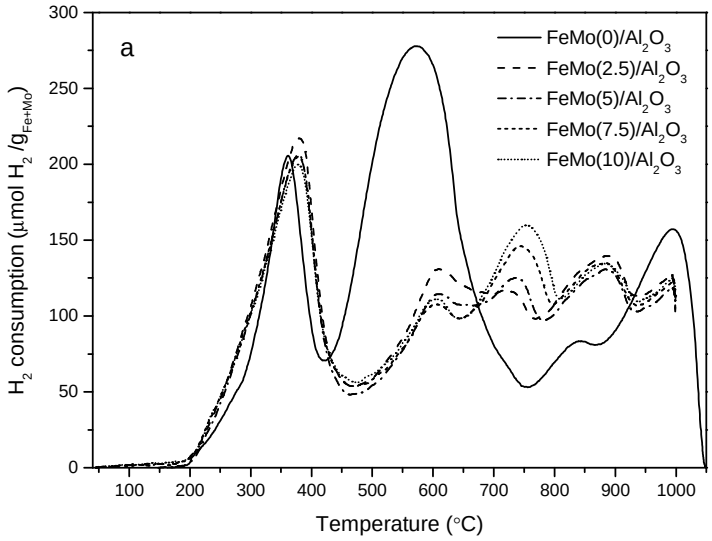
a
FeMo(0)/Al2O3
FeMo(2.5)/Al2O3
FeMo(5)/Al2O3
FeMo(7.5)/Al2O3
FeMo(10)/Al2O3
H2 consumption (μmol H2 /gFe+Mo)
Temperature (°C)

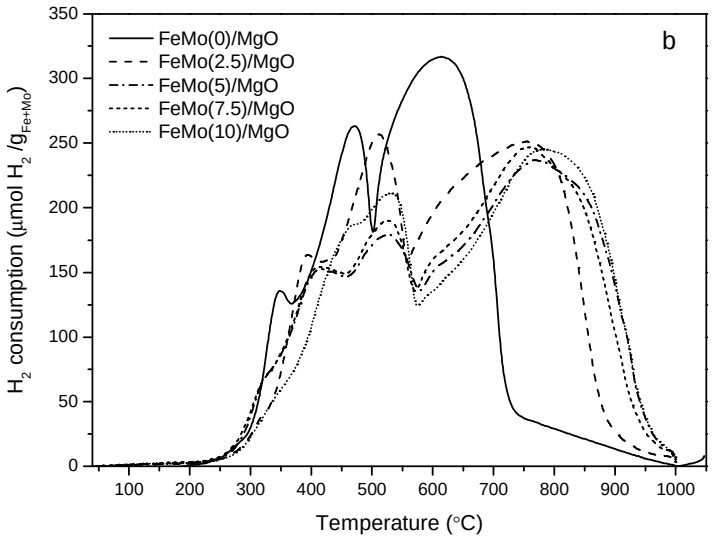
b
FeMo(0)/MgO
FeMo(2.5)/MgO
FeMo(5)/MgO
FeMo(7.5)/MgO
FeMo(10)/MgO
H2 consumption (μmol H2 /gFe+Mo)
Temperature (°C)

Figure 3.

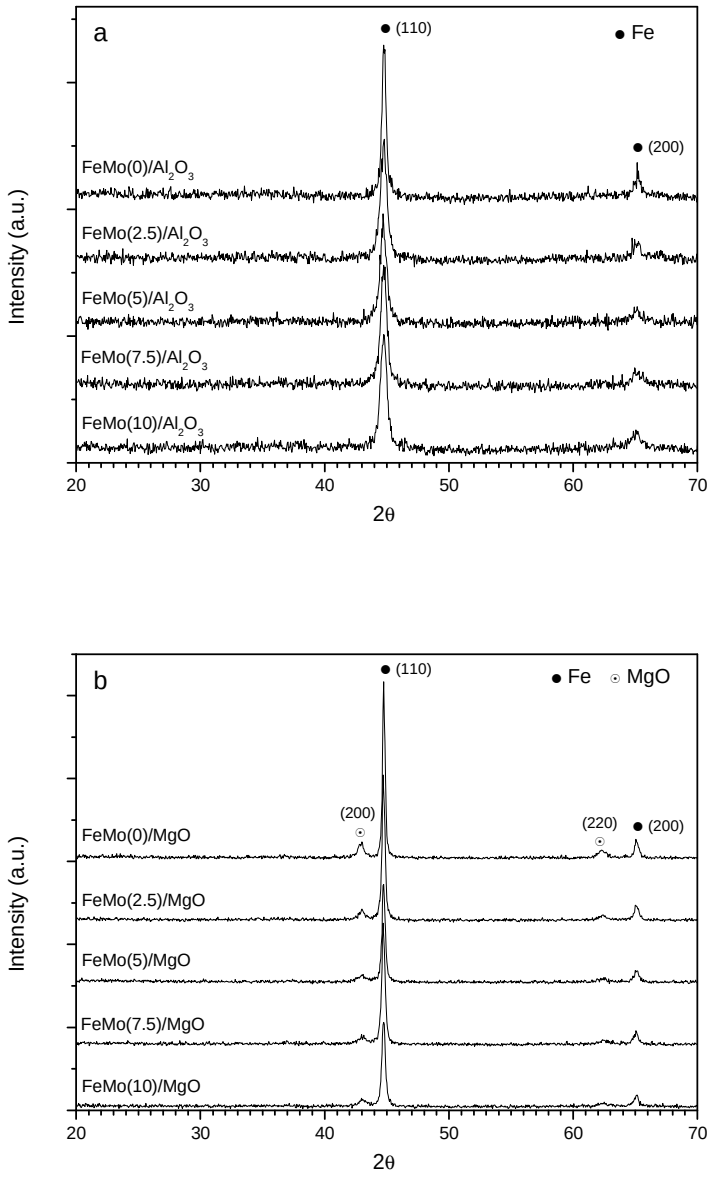
a
● (110)
● Fe
● (200)
FeMo(0)/Al2O3
FeMo(2.5)/Al2O3
FeMo(5)/Al2O3
FeMo(7.5)/Al2O3
FeMo(10)/Al2O3
Intensity (a.u.)
20
30
40
50
60
70
2θ
b
● (110)
● Fe
⊙ MgO
(200)
(220)
● (200)
FeMo(0)/MgO
FeMo(2.5)/MgO
FeMo(5)/MgO
FeMo(7.5)/MgO
FeMo(10)/MgO
Intensity (a.u.)
20
30
40
50
60
70
2θ

Figure 4.

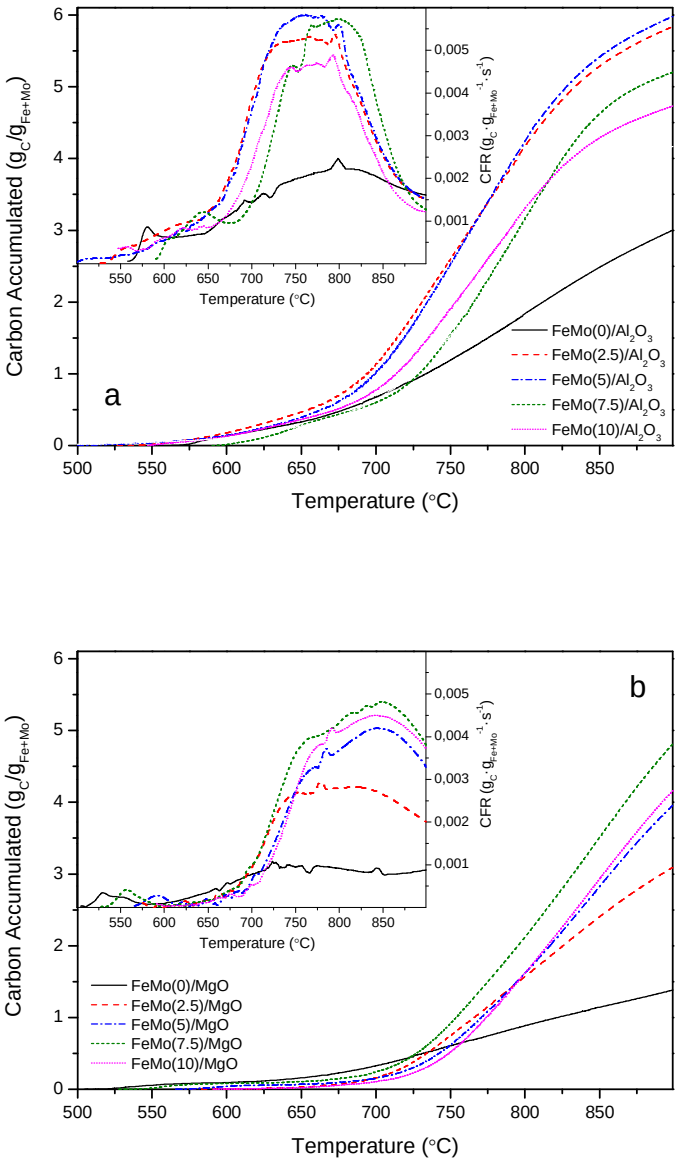
a
Carbon Accumulated (g_C/g_{Fe+Mo})
Temperature (°C)
CFR ($g_C \cdot g_{Fe+Mo}^{-1} \cdot s^{-1}$)
FeMo(0)/Al_2O_3
FeMo(2.5)/Al_2O_3
FeMo(5)/Al_2O_3
FeMo(7.5)/Al_2O_3
FeMo(10)/Al_2O_3
b
Carbon Accumulated (g_C/g_{Fe+Mo})
Temperature (°C)
CFR ($g_C \cdot g_{Fe+Mo}^{-1} \cdot s^{-1}$)
FeMo(0)/MgO
FeMo(2.5)/MgO
FeMo(5)/MgO
FeMo(7.5)/MgO
FeMo(10)/MgO

Figure 5.

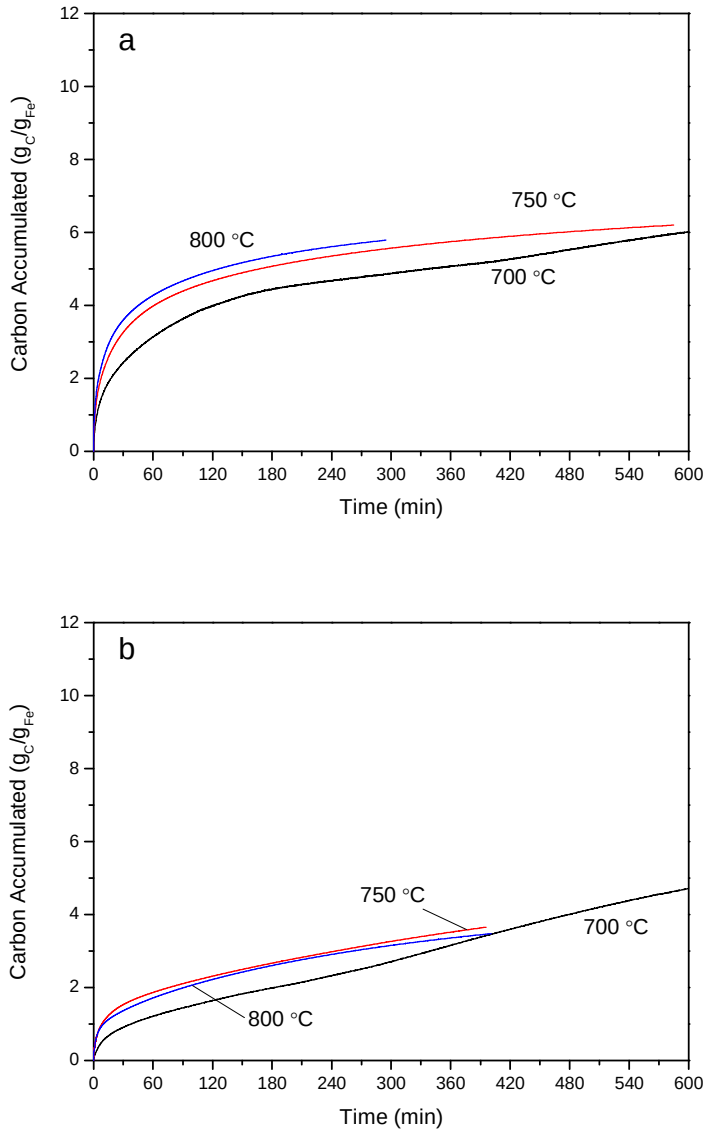
a
b
Carbon Accumulated (g_C/g_{Fe})
Time (min)
800 °C
750 °C
700 °C
0
2
4
6
8
10
12
0
60
120
180
240
300
360
420
480
540
600

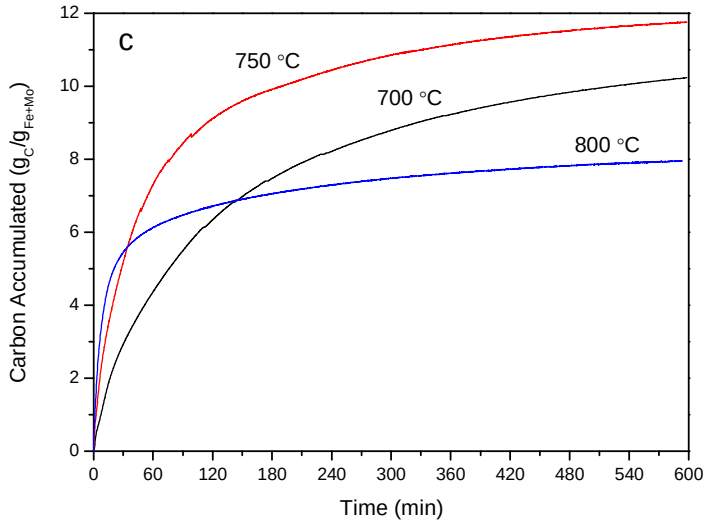
c
750 °C
700 °C
800 °C
Carbon Accumulated (g_C/g_{Fe+Mo})
Time (min)
0
2
4
6
8
10
12
0
60
120
180
240
300
360
420
480
540
600

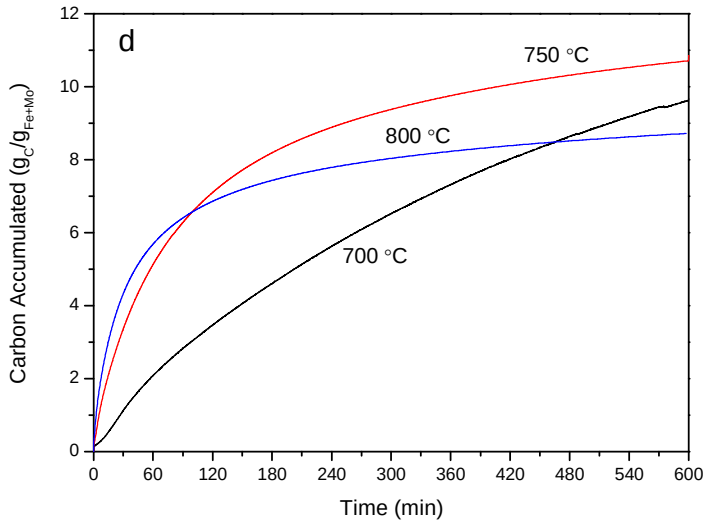
d
750 °C
800 °C
700 °C
Carbon Accumulated (g_C/g_{Fe+Mo})
Time (min)
0
2
4
6
8
10
12
0
60
120
180
240
300
360
420
480
540
600

Figure 6.

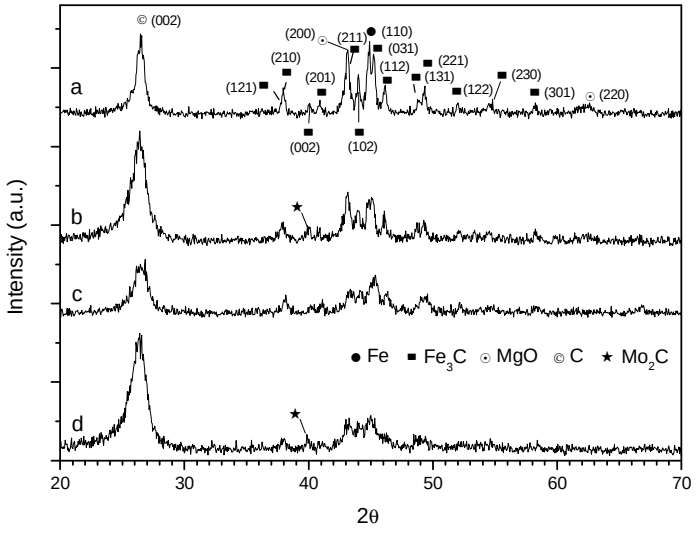
© (002)
(200) ⊙
(211)
● (110)
■ (031)
(210) ■
(112) ■
■ (221)
(121) ■
(201) ■
(131) ■
(122) ■
■ (230)
■ (301)
⊙ (220)
(002) ■
(102) ■
a
b
c
d
★
● Fe ■ Fe3C ⊙ MgO © C ★ Mo2C
Intensity (a.u.)
20
30
40
50
60
70
2θ

Figure 7.

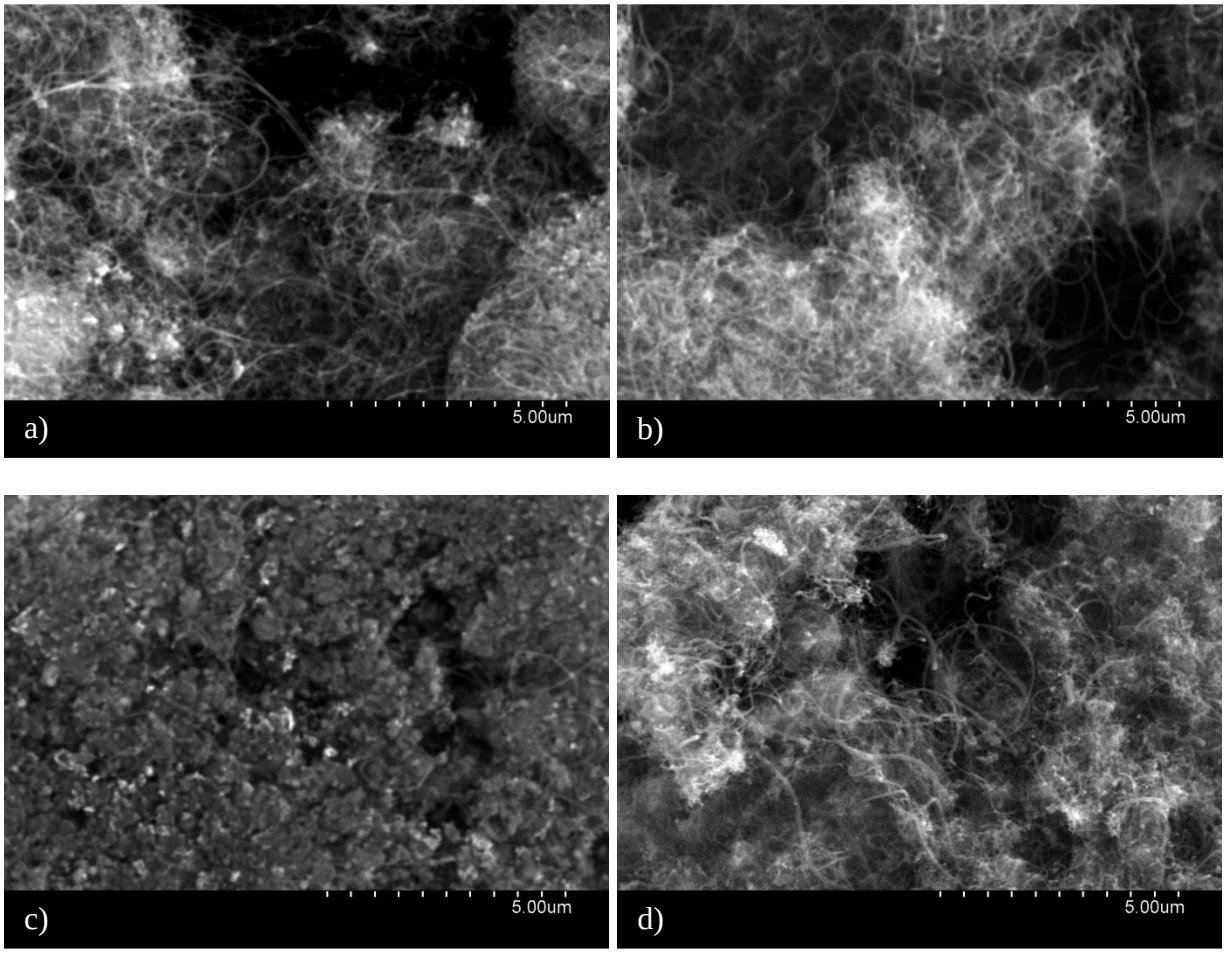

Figure 8.

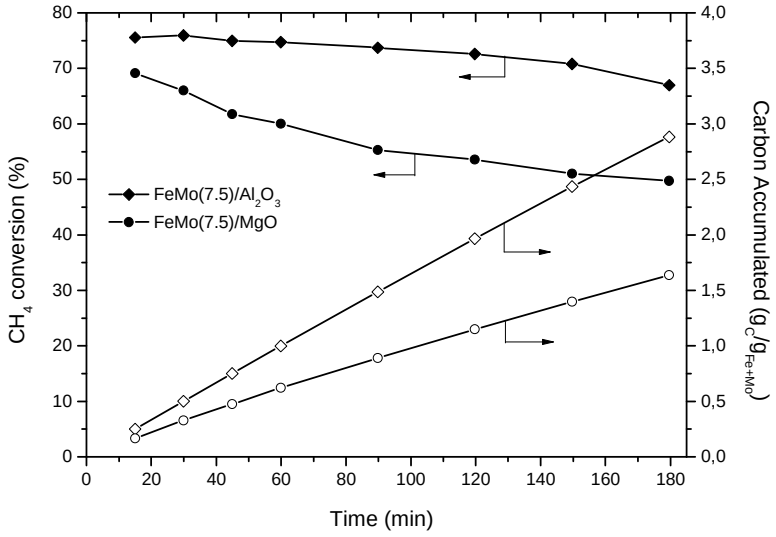
CH4 conversion (%)
Carbon Accumulated (gC/gFe+Mo)
Time (min)
FeMo(7.5)/Al2O3
FeMo(7.5)/MgO
0
10
20
30
40
50
60
70
80
0,0
0,5
1,0
1,5
2,0
2,5
3,0
3,5
4,0
0
20
40
60
80
100
120
140
160
180

Figure 9.

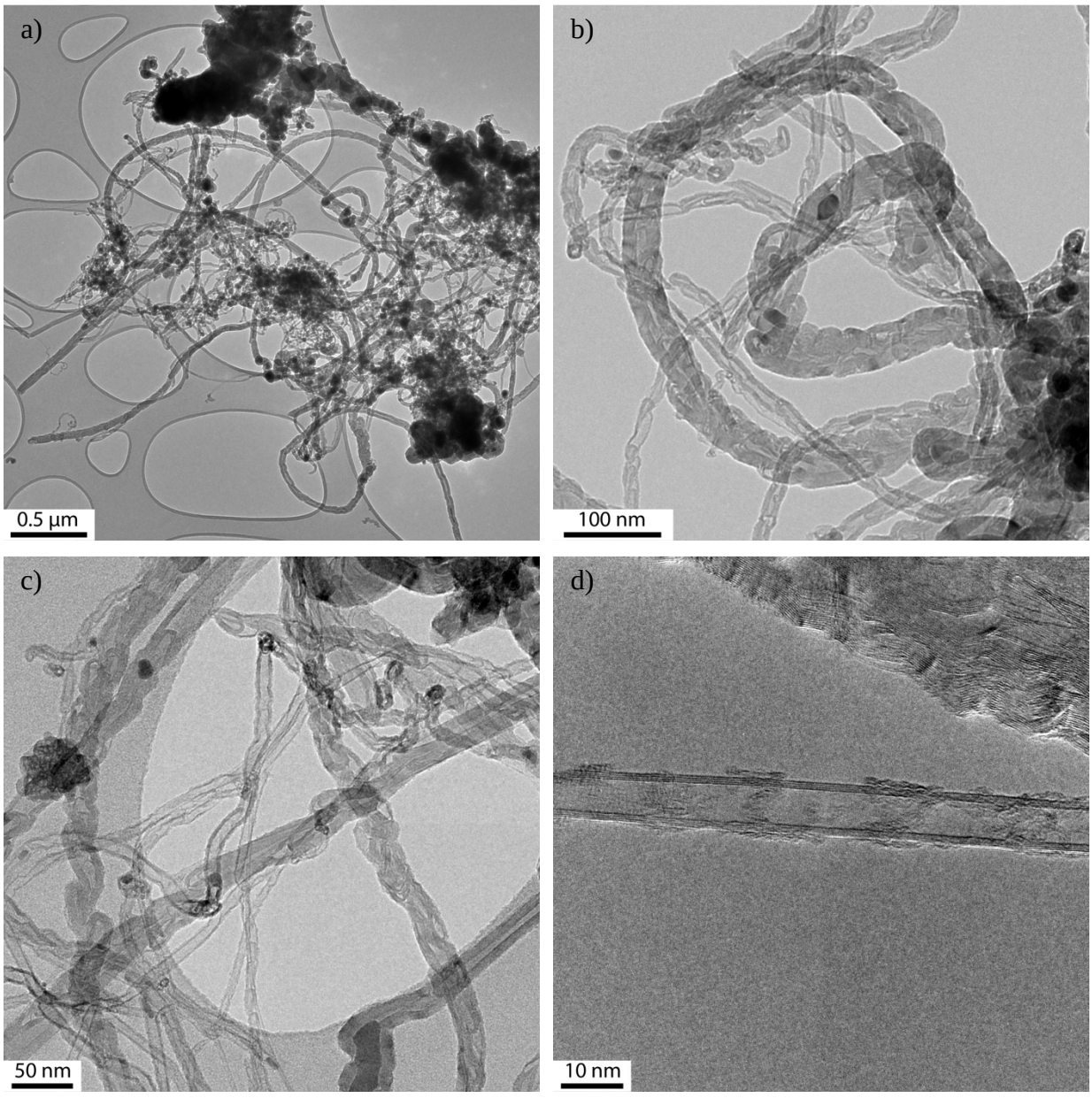

Figure 10.